

METHODS AND VERIFICATION OF THE NUMERICAL SOLUTIONS OF THE DIFFUSION EQUATIONS

The details of the numerical solutions of the 3-D diffusion equations in a right-circular cylinder and in one spatial dimension with continuously variable area of cross section and D are presented here. Several tests of the accuracy of the numerical methods are also presented.

Numerical solution of the 3-D model

Theory Eqs. 2 and 3 are parabolic partial differential equations (PDEs) with unspecified coordinates. Rods, in particular their OSs, are approximately right-circular cylinders; thus, solution of Eqs. 2–7 with respect to rods is most conveniently done in cylindrical coordinates. The PDEs describing the diffusion of the unphotoconverted, b , and photoconverted, c , forms of PAGFP with respect to an inhomogeneous source term in cylindrical coordinates are

$$\frac{\partial b}{\partial t} = D_r \left(\frac{\partial^2 b}{\partial r^2} + \frac{1}{r} \frac{\partial b}{\partial r} \right) + D_\theta \frac{1}{r^2} \left(\frac{\partial^2 b}{\partial \theta^2} \right) + D_z \left(\frac{\partial^2 b}{\partial z^2} \right) - Q, \quad (S1)$$

$$\frac{\partial c}{\partial t} = D_r \left(\frac{\partial^2 c}{\partial r^2} + \frac{1}{r} \frac{\partial c}{\partial r} \right) + D_\theta \frac{1}{r^2} \left(\frac{\partial^2 c}{\partial \theta^2} \right) + D_z \left(\frac{\partial^2 c}{\partial z^2} \right) + Q, \quad (S2)$$

where D_r , D_θ , and D_z are the diffusivities in the indicated directions.

Eqs. S1 and S2 are first order in t and second order in r , θ , and z . Therefore, one initial condition (IC) in t and two BCs (BCs) in each of the spatial variables r , θ , and z are required for each equation. The ICs given in Eq. 5 are restated here in cylindrical coordinates:

$$b(r, \theta, z, t \leq 0) = b_0 \quad (S3)$$

$$c(r, \theta, z, t \leq 0) = 0. \quad (S4)$$

The BCs in r were taken as:

$$\frac{\partial b(r=0, \theta, z, t)}{\partial r} = \frac{\partial b(r=r_0, \theta, z, t)}{\partial r} = 0 \quad (S5a,b)$$

$$\frac{\partial c(r=0, \theta, z, t)}{\partial r} = \frac{\partial c(r=r_0, \theta, z, t)}{\partial r} = 0, \quad (S6a,b)$$

which specify symmetry in r at $r=0$ and specify a no-flux boundary at the cell surface, $r=r_0$. The BCs in θ are:

$$\frac{\partial b(r, \theta=0, z, t)}{\partial \theta} = \frac{\partial b(r, \theta=\pi/2, z, t)}{\partial \theta} = 0 \quad (S7a,b)$$

$$\frac{\partial c(r, \theta=0, z, t)}{\partial \theta} = \frac{\partial c(r, \theta=\pi/2, z, t)}{\partial \theta} = 0, \quad (S8a,b)$$

which specify symmetry in θ at $\theta=0, \pi/2$ due to the symmetry of the source term and assuming isotropic diffusion in r and θ . The BCs in z are:

$$\frac{\partial b(r, \theta, z=l, t)}{\partial z} = \frac{\partial b(r, \theta, z=L, t)}{\partial z} = 0 \quad (S9a,b)$$

$$\frac{\partial c(r, \theta, z=l, t)}{\partial z} = \frac{\partial c(r, \theta, z=L, t)}{\partial z} = 0, \quad (S10a,b)$$

which specify a no-flux condition at the ends of the cylinder, $z=l, L$ (compare Fig. 2 B).

The numerical solution to Eqs. S1–S10 is accomplished through the method of lines (MOL), which replaces the PDEs specified by Eqs. S1 and S2 with ODE (finite difference) approximations of the derivatives with respect to r , θ , and z (Schiesser, 1991; Schiesser and Griffiths, 2009). To develop a numerical procedure, the inherent singularities at $r=0$ in Eqs. S1 and S2 must be regularized. For example, the first singularity in the radial term of Eq. S1 can be handled in the conventional way using l'Hospital's rule and Eq. S5a

$$\lim_{r \rightarrow 0} \frac{1}{r} \frac{\partial b}{\partial r} = \frac{\partial^2 b}{\partial r^2}. \quad (S11)$$

The second singularity in Eq. S1,

$$\lim_{r \rightarrow 0} \frac{1}{r^2} \left(\frac{\partial^2 b}{\partial \theta^2} \right),$$

appears not to have a readily available value in cylindrical coordinates. Thus, we reason that essentially what is required is the accurate calculation of the Laplacian (RHS) of Eq. S1 at the origin $r = 0$, which may be achieved in any suitable coordinate system. Therefore, we switch to Cartesian coordinates, in which there is a solution at $r = 0$, to accomplish this. The Laplacian in Cartesian coordinates is

$$\nabla^2 = \frac{\partial^2}{\partial x^2} + \frac{\partial^2}{\partial y^2} + \frac{\partial^2}{\partial z^2}. \quad (\text{S12})$$

For Eq. S1 at the general grid point $p(i, j, k)$, where i, j , and k are the indices for r, θ , and z , respectively, the spatial derivatives are approximated as

$$\frac{\partial^2 b}{\partial r^2} + \frac{1}{r} \frac{\partial b}{\partial r} \approx \frac{b(i+1, j, k) - 2b(i, j, k) + b(i-1, j, k)}{\Delta r^2} + \frac{1}{r(i, j, k)} \cdot \frac{b(i+1, j, k) - b(i-1, j, k)}{2\Delta r} \quad (\text{S13a})$$

$$\frac{1}{r^2} \frac{\partial^2 b}{\partial \theta^2} \approx \frac{1}{r(i, j, k)^2} \frac{b(i, j+1, k) - 2b(i, j, k) + b(i, j-1, k)}{\Delta \theta^2} \quad (\text{S13b})$$

$$\frac{\partial^2 b}{\partial z^2} \approx \frac{b(i, j, k+1) - 2b(i, j, k) + b(i, j, k-1)}{\Delta z^2} \quad (\text{S13c})$$

and the inhomogeneous source term is

$$\begin{aligned} Q_s &= \alpha_m^* \gamma^* I^m(i, j, k, t) b, & 0 \leq t \leq \Delta T \\ &= 0, & t \geq \Delta T. \end{aligned} \quad (\text{S13d})$$

Substitution of Eq. S13 in Eq. S1 gives a system of $n_r \times n_\theta \times n_z$ ODEs in t . The left-hand side of Eq. S1 is the derivative $db(i, j, k) / dt$, for which the IC is Eq. S3.

Numerical solution of the 1-D model with variable $A(z)$ and $D(z)$

The mass balance for a rod cell idealized as a 1-D cylinder, with axial coordinate z , variable diffusion coefficient $D(z)$, and cross-sectional area $A(z)$ (Eq. 13) may be expressed as:

$$A(z)\Delta z \frac{\partial c}{\partial t} = -A(z)D(z) \frac{\partial c}{\partial z} \Big|_z - \left[-A(z)D(z) \frac{\partial c}{\partial z} \Big|_{z+\Delta z} \right], \quad (\text{S14})$$

where $A(z)\Delta z \partial c / \partial t$ is the accumulation or depletion (depending on the sign of $\partial c / \partial t$) of protein in an incremental volume $A(z)\Delta z$, and $-A(z)D(z) \partial c / \partial z|_z$ is the rate of diffusion into or out of (depending on the sign of $\partial c / \partial z$) the infinitesimal spatial position z according to Fick's first law. Similarly, $-A(z)D(z) \partial c / \partial z|_{z+\Delta z}$ is the rate of diffusion into or out of the infinitesimal spatial position $z + \Delta z$. Thus, the difference in these two terms is the net rate of mass transfer into or out of the incremental volume due to diffusion. Division of Eq. S14 by $A(z)\Delta z$ with minor rearrangement gives

$$\frac{\partial c}{\partial t} = \frac{A(z)D(z) \frac{\partial c}{\partial z} \Big|_{z+\Delta z} - A(z)D(z) \frac{\partial c}{\partial z} \Big|_z}{A(z)\Delta z}. \quad (\text{S15})$$

In the limit $\Delta z \rightarrow 0$, Eq. S15 becomes

$$\frac{\partial c}{\partial t} = \frac{1}{A(z)} \frac{\partial \left[A(z)D(z) \frac{\partial c}{\partial z} \right]}{\partial z}. \quad (\text{S16})$$

Initial and BCs

Either of two sets of BCs were used in the solution of Eq. S16:

$$\frac{\partial c(0, t)}{\partial z} = \frac{\partial c(L, t)}{\partial z} = 0 \quad (\text{S17})$$

or

$$c(0, t) = f(t), \frac{\partial c(L, t)}{\partial z} = 0. \quad (\text{S18})$$

The two homogeneous (0) Neumann BCs of Eq. S17 specify 0 flux of the protein through the boundaries at $z = 0, L$. The Dirichlet (first) BC of Eq. S18 specifies the concentration of the protein at $z = 0$ as a time-dependent function $f(t)$. The homogeneous Neumann (second) BC at $z = L$ specifies 0 flux of the protein through the boundary $z = L$. Finally, Eq. S16 also requires one IC, which is

$$c(z, 0) = c_0(z), \quad (\text{S19})$$

where $c_0(z)$ is an initial distribution of the protein.

Solution

Eqs. S17–S19 were solved numerically by the MOL. The z dimension of the rod was divided into n spatial positions with index i , and the derivatives in z were approximated by finite differences, which converts them into algebraic expressions, leaving only the derivative in t . Thus, ODEs in t remain. At grid point i , the MOL approximation of Eq. S16 is

$$\begin{aligned} \frac{dc_i}{dt} = & \frac{1}{A(z_i)} \cdot \left[\frac{A(z_{i+1})D(z_{i+1}) + A(z_i)D(z_i)}{2} \left(\frac{c_{i+1} - c_i}{z_{i+1} - z_i} \right) - \dots \right. \\ & \left. - \frac{A(z_i)D(z_i) + A(z_{i-1})D(z_{i-1})}{2} \left(\frac{c_i - c_{i-1}}{z_i - z_{i-1}} \right) \right] \cdot \\ & \left[\frac{1}{(z_{i+1} + z_i) / 2 - (z_i + z_{i-1}) / 2} \right] \end{aligned} \quad (\text{S20})$$

for $i = 1, \dots, n$. For the first of the BCs (Eqs. S17 and S20) becomes

$$\frac{dc_1}{dt} = \frac{1}{A(z_1)} \cdot \left[\frac{A(z_2)D(z_2) + A(z_1)D(z_1)}{2} \left(\frac{c_2 - c_1}{z_2 - z_1} \right) \right] \cdot \left[\frac{1}{z_2 - z_1} \right], \quad (\text{S21})$$

where the flux between $i = 0$ (a fictitious point) and $i = 1$ is taken to be 0. Similarly, Eq. S20 for the no-flux BC of Eq. S17 at $z = L$ is

$$\begin{aligned} \frac{dc_n}{dt} = & \frac{1}{A(z_n)} \cdot \left[- \frac{A(z_n)D(z_n) + A(z_{n-1})D(z_{n-1})}{2} \left(\frac{c_n - c_{n-1}}{z_n - z_{n-1}} \right) \right] \cdot \\ & \left[\frac{1}{z_n - z_{n-1}} \right], \end{aligned} \quad (\text{S22})$$

where the flux between the fictitious point $i = n + 1$ and $i = n$ is taken to be 0.

For the Dirichlet BC of Eq. S18 at $z = 0$, the ODE at grid point $i = 1$ is

$$\frac{dc_1}{dt} = \frac{df(t)}{dt}, \quad (\text{S23})$$

and the Neumann BC of Eq. S18 at $z = L$ is the same as Eq. S22.

The ODEs are integrated forward in t from $t = 0$ using a MATLAB ODE integrator, e.g., `ode15s`, starting from the IC of Eq. S19.

Verification of the solutions

The numerical solutions obtained were verified using three criteria as follows.

Grid density: mass conservation

An important consideration in numerical approximations of PDE systems is the appropriate grid density. The density should be sufficient to provide an accurate solution, but not so dense that the time required to run the code becomes prohibitively long. Good indicators of accurate solutions are the maintenance of constant mass

of the diffusing substance and solution convergence over the time course of the calculation. The total mass of components b and c was computed by an approximation to the integral based on the differential volume $rd\theta dr dz$

$$\begin{aligned} M(t) = & \int_0^L \int_0^{\eta} \int_0^{2\pi} [b(r, \theta, z, t) + c(r, \theta, z, t)] rd\theta dr dz \\ \approx & \sum_{k=1}^{n_z-1} \sum_{j=1}^{n_\theta-1} \sum_{i=1}^{n_r-1} [b(i, j, k) + b(i+1, j, k) + b(i, j+1, k) \\ & + b(i, j, k+1) + c(i, j, k) + c(i+1, j, k) + c(i, j+1, k) \\ & + c(i, j, k+1)] / 4[r(i) + r(i+1)] / 2\Delta\theta\Delta r\Delta z, \end{aligned} \quad (\text{S24})$$

where $\Delta\theta$, Δr , and Δz are the finite difference increments in θ , r , and z , respectively.

We find that the most important consideration in determining appropriate grid density that maintains constant mass is that the source term (Q , Eq. 4) be adequately represented spatially with best results obtained when Q is at least eightfold over sampled in the radial and axial dimensions. In terms of the dimensions of the *psf*, which is described as a Gaussian profile with $\sigma_{x,z} = 0.16 \mu\text{m}$, this means the best results were obtained with a grid density of $8/0.32 = 25$ grid points per μm . At this density, mass was conserved to three significant figures.

As a matter of practicality, in a cylindrical OS $40\text{-}\mu\text{m}$ long with $r = 3 \mu\text{m}$, and θ sampled at 10-degree increments, the number of ODEs ($n_r \times n_\theta \times n_z$) calculated for each time point at this grid density was $75 \times 36 \times 1,000 = 2.7 \times 10^6$. Symmetry allows eightfold reduction in this number by calculating a single octant of the 3-D space.

Grid density: solution convergence

Solution accuracy was directly checked by varying the grid density in r , θ , and z . Increasing the density beyond that required for the mass balance did not materially improve the convergence beyond three significant figures.

Comparison to cases with tractable analytical solutions

To assess the accuracy of the numerical solutions, spatial geometries, ICs, and BCs may be chosen that allowed analytical solutions that then may be compared with the various solutions obtained by the MOL. In the case of the 3-D right-circular cylinder (Eqs. 2–7), relevant analytical solutions are most conveniently obtained via Green's functions with ICs defined by the Dirac delta function. Such solutions are readily found in Carslaw and Jaeger (1959) or Polyanin (2001). Comparisons of MOL to analytical solutions obtained as such have been

examined in detail previously and shown to be identical to three significant figures (Schiesser and Griffiths, 2009).

To test the accuracy of the numerical 1-D model described by Eqs. 13–15, we examined diffusion equations for a right-circular cylinder (constant $A(z)$, identical to the slab) with axial dimension, z , boundaries at $z = 0$ and $z = L$, and with the following initial and BCs:

$$\begin{aligned} c(z, t = 0) &= 0 \\ c(z = 0, t) &= f(t) \\ \frac{\partial c(z = L, t)}{\partial z} &= 0, \end{aligned} \quad (\text{S25})$$

where $f(t) = C(1 - \exp(-kt))$, C is the maximum concentration, and k is the time constant of concentration change. The diffusion equations with these ICs and BCs may be

solved using Duhamel's theorem, which allows analytical solution of PDEs with time-dependent terms. The solution is (Carslaw and Jaeger, 1959)

$$\begin{aligned} c(z, t) &= C - C \exp(-kt) \frac{\cos z(k/D)^{1/2}}{\cos l(k/D)^{1/2}} - \\ &\quad - \frac{16kCl^2}{\pi} \sum_{n=0}^{\infty} \frac{(-1)^n \exp(-D(2n+1)^2 \pi^2 t / 4L^2)}{(2n+1)[4kL^2 - D\pi^2(2n+1)^2]} \cos \frac{(2n+1)\pi z}{2L}. \end{aligned} \quad (\text{S26})$$

The numerical solution of Eqs. 13–15 with the BCs stated in Eq. S25 is identical to the analytical solution (Eq. S26) to three figures (Fig. S1). Additional verification procedures may be found in Calvert et al. (2007).

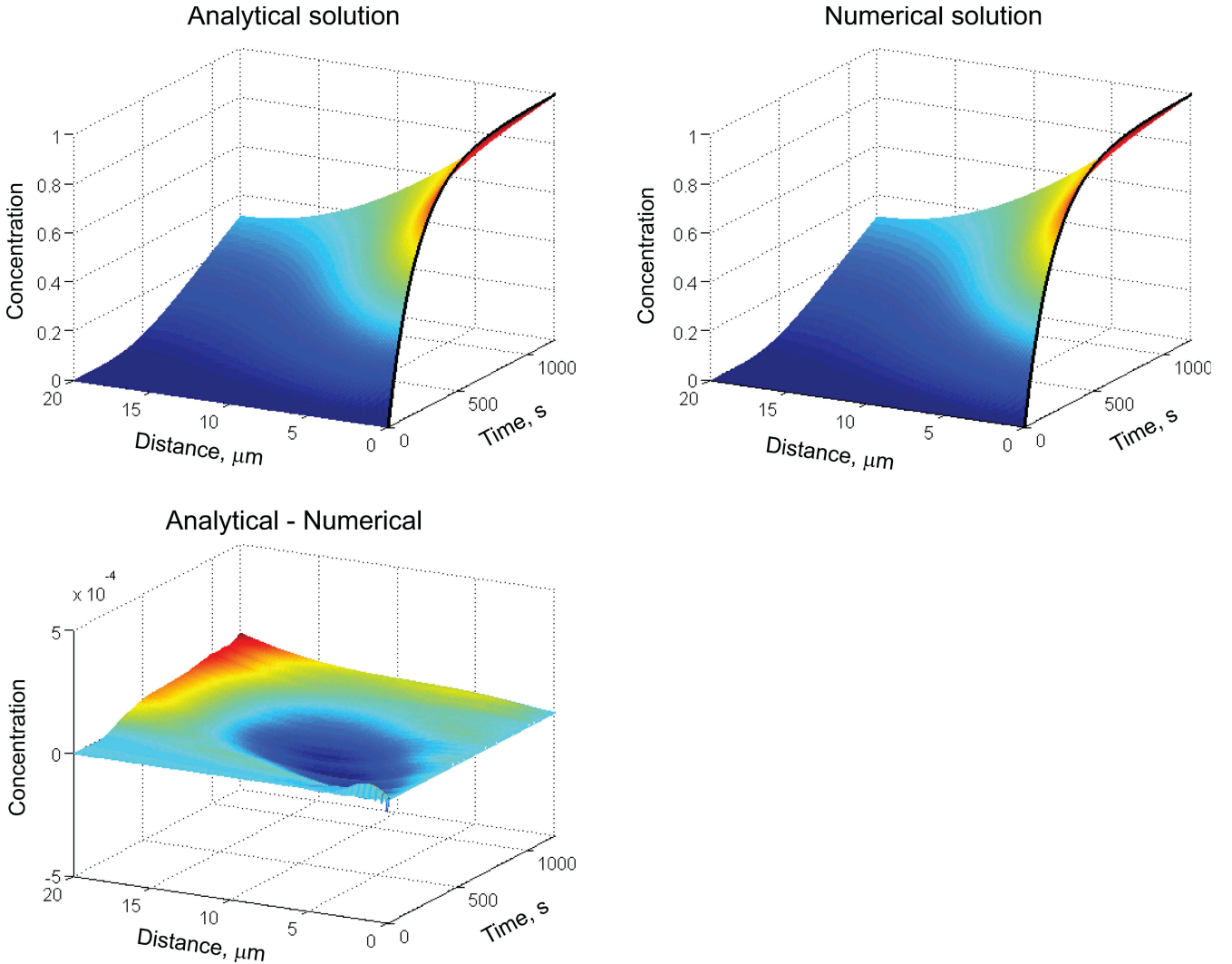


Figure S1. Comparison of analytical and numerical solutions to diffusion in a cylinder with a time varying Dirichlet BC at $z = 0$. The analytical solution used $k = 0.005 \text{ s}^{-1}$ and $C = 1$ in Eq. S26. The numerical solution used an exponential function with the same constants implemented as a Dirichlet BC; $D = 0.10 \text{ } \mu\text{m}^2 \text{ s}^{-1}$. The maximum absolute difference was 1.35 e-4 (0.0135%).

Data analysis details

RMS Error optimization of estimates of D . Estimates of diffusion coefficients were optimized by calculating the root-mean-square difference error E_{RMS} between fluorescence data and model prediction. In the case of the point blast line scan protocol of Fig. 9, where the 3-D cylinder model was used, this was calculated as

$$E_{RMS} = \left[\frac{\sum_r \sum_t (F'(r,t) - F_m(r,t))^2}{n_{pts}} \right]^{0.5}, \quad (S27)$$

and in the case of the 1-D model, this was calculated as

$$E_{RMS} = \left[\frac{\sum_z \sum_t (F'(z,t) - F_M(z,t))^2}{n_{pts}} \right]^{0.5}, \quad (S28)$$

where F' is the spatiotemporal profile of water space-corrected fluorescence, F_M is the fluorescence profile

predicted by the model, and n_{pts} is the total number of values in the spatiotemporal profile.

Determination of cell dimensions. Determination of the dimension of the cell being examined, particularly with respect to the CC and its relationship to the IS–OS transition, is crucial to the analysis of molecular diffusion. The dimensions of the cells were determined from 3-D scans of the cells at the beginning or end of a given experiment. The cell of interest was cut from the image stack using a 3-D “cookie-cutting” routine described previously (Peet et al., 2004). Individual intensity images in the x – z dimension (where here z refers to the direction of the optical path) were deconvolved with a kernel derived from the measured 3-D point spread function (psf) to remove the blurring inherent to confocal and multiphoton imaging, after which the edges of the cell were detected using the Canny method (available in the MATLAB Image Processing Toolbox). To obtain a cell’s area of cross section as a function of the axial, z dimension, the areas of the pixels identified as being within the cell boundary for each x – z image were integrated (Fig. S2).

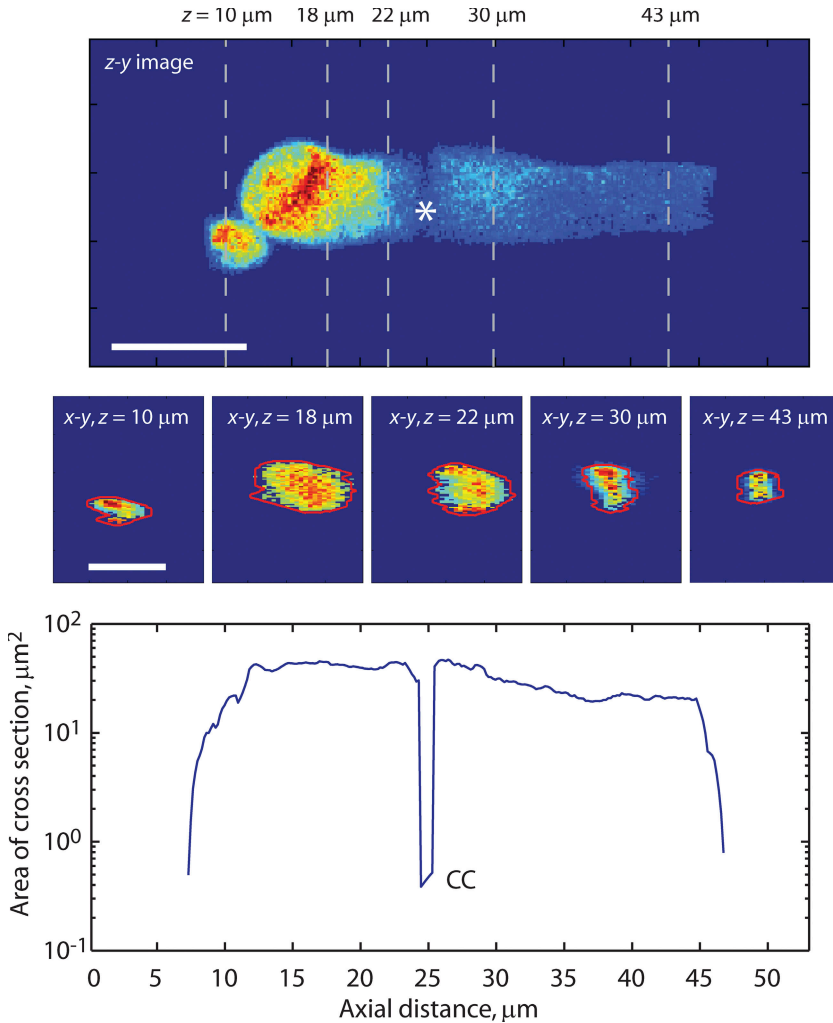


Figure S2. Determination of the area of cross section as a function of axial position. (Top) Central z – y image from a 3-D image stack of a rod expressing PAGFP. (Middle) x – y cross sections from the indicated z positions illustrate the edge detection protocol (red line). The areas of each pixel within the detected cross section are integrated to arrive at the area of cross section for a given z position. (Bottom) Logarithm of the areas of cross section plotted as a function of distance in z . CC indicates the area of cross section of the CC that was inserted at the IS–OS transition as determined by visual inspection of the projection image (indicated by white asterisk in top panel).

The cross section of the CC cannot be determined with confocal or multiphoton microscopy because its size is below the resolution limits of these methods. Instead, the lengths and diameters of the connecting cilia from six *Xenopus* rods were determined from transmission electron micrographs, the average results of which are given in Table I. From these data, we derived an average CC cross-sectional area as a function of axial dimension that we then inserted into the cross-sectional area array at an axial position determined from visual inspection of the fluorescent image of the cell (Fig. S2). A complete quantitative description of the plasma membrane-delimited dimensions of the individual cell under investigation was thus generated.

Analysis of PAGFP concentration effects on estimation of D

The concentration of PAGFP in the rods examined was estimated as described in Peet et al. (2004). In brief, the average fluorescence of the brightest 5% of voxels in a cell was determined and assumed to represent the voxels with the least volume occupied by subcellular structures before photoactivation. The PAGFP concentration was then obtained with the following equation (cf. Peet et al., 2004):

$$[PAGFP]_{cell} = \frac{F}{K \cdot I_{max} \cdot 10^{-ndf}}, \quad (S29)$$

where F is the mean fluorescence of the brightest 5% voxels, I_{max} is the intensity of the unattenuated 488-nm laser, ndf is the calibrated density of the neutral density filter used to attenuate the laser during cell imaging, and K is a system constant obtained from measurements with

recombinant protein. For calibration of rPAGFP concentration, we assumed an extinction coefficient of $\epsilon_{400} = 20,700$ (Patterson and Lippincott-Schwartz, 2002).

Does local binding significantly impact estimation of D_{PAGFP} in rod cells?

The range of PAGFP concentrations in the cells we examined spanned 2.3 decades, and yet D_{CC} did not correlate with PAGFP concentration (Fig. S3). This strongly argues against significant binding of PAGFP, although it does not rule out weak binding that may have a small impact on PAGFP diffusion.

Does self-crowding significantly impact estimation of D_{PAGFP} in rod cells?

We determined the level of self-crowding produced by the measured concentrations. The mean distance, d , between PAGFP molecules may be calculated as:

$$d = c^{-1/3}, \quad (S30)$$

where c is the concentration expressed in molecules/distance³ (at the high end of the concentration range examined, $\sim 100 \mu\text{M}$, $d = 25.5 \text{ nm}$). Self-crowding does not appear to significantly affect diffusion of macromolecules until the volume fraction occupied by the molecules exceeds $\sim 10\%$ (See Dix and Verkman, 2008 and Zhou et al., 2008). GFP is an approximately barrel-shaped molecule with dimensions of $\sim 4.2\text{-nm}$ long and $\sim 2.4 \text{ nm}$ in diameter, and thus occupies a volume of 19 nm^3 . The spacing of PAGFPs in the highest expressing cells we examined ($d = 25.5 \text{ nm}$) means that on average, each PAGFP is surrounded by a volume of $16,581 \text{ nm}^3$ within which no other PAGFP molecule resides, produc-

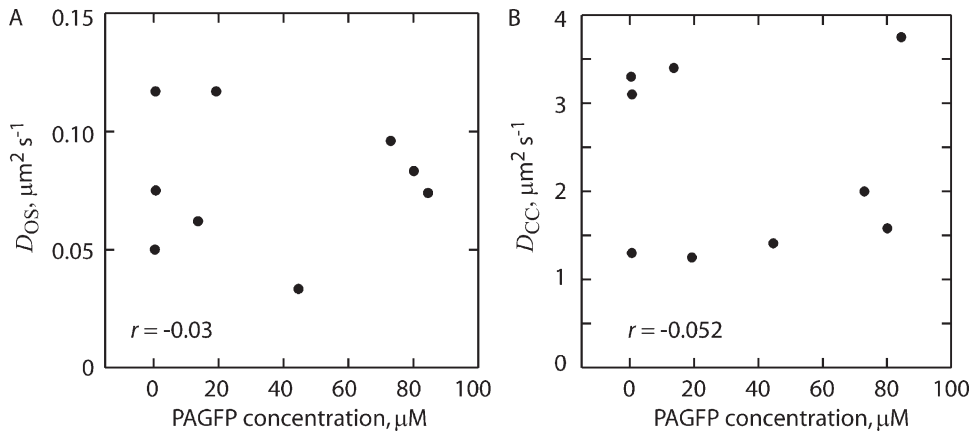


Figure S3. Test of the hypothesis that PAGFP diffusion coefficients correlate with PAGFP concentration. D_{OS} (A) and D_{CC} (B) values were plotted as a function of PAGFP concentration determined in the IS before photoconversion. Linearity of the relationships was assessed by computing sample correlation coefficients, r , which were found to be -0.052 and -0.03 for the CC and OS, respectively, indicating no correlation of D with concentration in either compartment.

ing a volume ratio of 0.1%. This clearly argues against self-crowding having a significant impact on the apparent PAGFP diffusion coefficients measured in rods.

Advection/diffusion model of soluble protein transport

Advection is the process of fluid flow caused by some generating force, such as vesicles being transported through the narrow CC lumen. An advective component may be introduced into Eq. 13 of Theory to yield the advection/diffusion PDE,

$$\frac{\partial c}{\partial t} = \frac{1}{A(z)} \frac{\partial \left(A(z) \cdot D(z) \cdot \frac{\partial c}{\partial z} \right)}{\partial z} - \frac{1}{A(z)} \frac{\partial (A(z)v(z)c)}{\partial z}, \quad (\text{S31})$$

where the additional term includes $v(z)$, the velocity of the advective flow in units of distance per time. The boundary and initial conditions, respectively, are

$$\begin{aligned} \frac{\partial c(z=l, t)}{\partial z} &= \frac{\partial c(z=L, t)}{\partial z} = 0 \\ c(z, t=0) &= c_0(z). \end{aligned} \quad (\text{S32})$$

Eqs. S31 and S32 were solved using the numerical MOL similarly as described for Eqs. 13–15 (Theory and see above). The magnitude of the flow velocity used, $1 \mu\text{m s}^{-1}$, was based on the vesicle transport rate necessary to supply the OS disc membranes with rhodopsin at a suitable density and the volume of the CC, derived from EM data in Table I, which provided a volumetric displacement as a function of time. Solutions were obtained for the system Eqs. S31 and S32 with varying values of D_{CC} and uniform initial concentration of transported species for all z over time long enough to achieve a steady state.

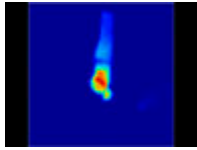
When D_{CC} was large ($>10 \mu\text{m}^2 \text{s}^{-1}$), the steady-state concentration distribution was similar to that found experimentally and with that of the diffusion-only model (uniform in the OS and IS compartments); thus, advection had little effect on transport. If D_{CC} was equal to the value estimated from the diffusion-only model ($2\text{--}3 \mu\text{m}^2 \text{s}^{-1}$), the steady-state concentration in the OS compartment exceeded that in the IS by 1.4–1.6-fold. For small D_{CC} values ($\leq 1 \mu\text{m}^2 \text{s}^{-1}$), the concentration in the OS compartment exceeded that in the IS from 2.6-fold up to the case where nearly all of the mass of the transported species collected in the OS. Thus, in the presence of diffusion and advection in the IS to OS direction, the concentration of PAGFP is predicted to be nonuniform, with higher concentrations predicted for the OS compartment. This result is consistent with a straightforward expectation based on an analysis of the flux of PAGFP through the CC. At steady state, there can be no net flux through the CC, and so throughout the CC we must have

$$q(z) = -vc(z) + D_{\text{CC}} \frac{dc}{dz} = 0, \quad (\text{S33})$$

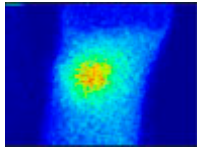
where v is the advective velocity. The solution of this equation predicts that the concentration of the diffusing species on the OS side of the CC (c_{OS}) is related to the that on the IS side (c_{IS}) by

$$c_{\text{OS}} = c_{\text{IS}} \exp\left[\frac{(z_{\text{OS}} - z_{\text{IS}})}{D_{\text{CC}} / v}\right]. \quad (\text{S34})$$

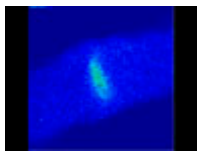
(Note that at steady state, concentrations within each of the OS and IS compartments must be uniform, although they are not necessarily equal.) The steady-state predictions of the advective/diffusion model (Eqs. S31 and S32) agree to within a few percent of the prediction of Eq. S34.



Video 1. PAGFP equilibration throughout rod photoreceptor cytoplasm. Frames acquired at 10-s intervals. Video playback at 10 frames per second.



Video 2. PAGFP diffusion in the IS. Frames acquired at 6.3 frames per second. Video playback at 10 frames per second.



Video 3. PAGFP diffusion in the OS. Frames acquired at 6 frames per second. Video playback at 10 frames per second.

REFERENCES

- Calvert, P.D., J.A. Peet, A. Bragin, W.E. Schiesser, and E.N. Pugh Jr. 2007. Fluorescence relaxation in 3D from diffraction-limited sources of PAGFP or sinks of EGFP created by multiphoton photoconversion. *J. Microsc.* 225:49–71. doi:10.1111/j.1365-2818.2007.01715.x
- Carslaw, H.S., and J.C. Jaeger. 1959. Conduction of Heat in Solids. Second edition. Oxford University Press, New York. 510 pp.
- Dix, J.A., and A.S. Verkman. 2008. Crowding effects on diffusion in solutions and cells. *Annu Rev Biophys.* 37:247–263. doi:10.1146/annurev.biophys.37.032807.125824
- Patterson, G.H., and J. Lippincott-Schwartz. 2002. A photoactivatable GFP for selective photolabeling of proteins and cells. *Science.* 297:1873–1877. doi:10.1126/science.1074952
- Peet, J.A., A. Bragin, P.D. Calvert, S.S. Nikonov, S. Mani, X. Zhao, J.C. Besharse, E.A. Pierce, B.E. Knox, and E.N. Pugh Jr. 2004. Quantification of the cytoplasmic spaces of living cells with EGFP reveals arrestin-EGFP to be in disequilibrium in dark adapted rod photoreceptors. *J. Cell Sci.* 117:3049–3059. doi:10.1242/jcs.01167
- Polyanin, A.D. 2001. Handbook of Linear Partial Differential Equations for Engineers and Scientists. Chapman & Taylor & Francis, London. 1544 pp.
- Schiesser, W.E. 1991. The numerical method of lines: integration of partial differential equations. Elsevier Academic Press, New York. 326 pp.
- Schiesser, W.E., and G.W. Griffiths. 2009. A compendium of partial differential equation models: method of lines analysis with MATLAB. Cambridge University Press, New York. 474 pp.
- Zhou, H.X., G. Rivas, and A.P. Minton. 2008. Macromolecular crowding and confinement: biochemical, biophysical, and potential physiological consequences. *Annu Rev Biophys.* 37:375–397. doi:10.1146/annurev.biophys.37.032807.125817